Characterisation of MX Precipitate Density and Irradiation Hardening in Advanced Reduced-Activation Ferritic-Martensitic Fusion Steels

James S.K-L. Gibson*[1], Alex Carruthers[1], Benjamin R. S. Evans[1], Jack Haley[1], Slava Kuksenko[1], Kay Song[2], Luke Hewitt[1], Stephen Jones[3], Shahin Mehraban[3], Nicholas Lavery[3], David Bowden[1]

Corresponding Author: james.gibson2@ukaea.uk

[1]Materials Division, United Kingdom Atomic Energy Authority, Culham Campus, Abingdon, United Kingdom

[2]Department of Materials, University of Oxford, Oxford, United Kingdom

[3]MACH1: Materials Advanced Characterisation Centre, Faculty of Science and Engineering, Swansea University, United Kingdom

Abstract

Reduced activation ferritic-martensitic (RAFM) steels are a recent class of radiation-resistant steels designed for the structural components of power-producing fusion reactors. In this work an advanced (A)RAFM steel has been developed with superior radiation hardening resistance with respect to the EUROFER-97 upon which it was based.

4D-STEM (scanning transmission electron microscopy) has been combined with a novel processing methodology to visualise all the fine MX precipitates that led to this outstanding radiation hardening resistance and determine a precipitate density of 5×10^{22} m^{-3}.

Self-ion irradiation campaigns up to 100 dpa at 350 °C show an increase in hardness of only 35% at 10 dpa where EUROFER-97 exhibits a near-doubling of its hardness. The initial work hardening response, as determined from spherical nanoindentation, is unchanged between the as-received state and irradiation to 100 dpa, implying that the alloy should retain reasonable ductility under these conditions. Proton irradiations at 250 °C, 350 °C, and 400 °C demonstrate that the low temperature hardening embrittlement threshold of the new steel is largely unaffected, increasing by only ~50 °C with respect to EUROFER-97.

A refinement of alloy chemistry and a subsequent modification of the thermomechanical treatments to favour MX precipitates is therefore a very promising strategy for the further development of fusion steels.

Keywords: Ferritic Steels, Fusion Energy, Mechanical Behaviour, Nanoindentation, STEM

Graphical Abstract

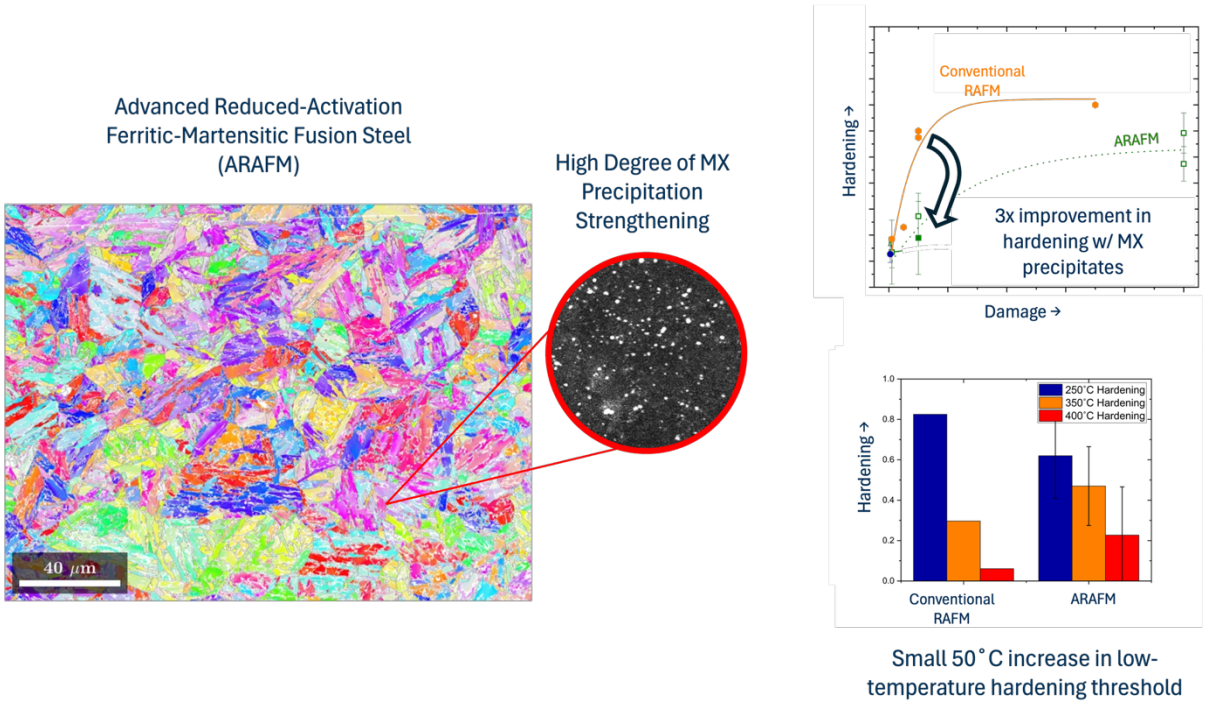

1. Introduction

Reduced activation ferritic-martensitic (RAFM) steels are a recent class of radiation-resistant steels designed to be used as the structural components of power-producing fusion reactors. Their goal is to provide high-temperature strength and creep resistance while consisting only of alloying elements that do not produce long-lived intermediate-level radioactive waste after use to reduce cooldown waiting periods for maintenance. The current generation of RAFM steels are limited to operating temperatures below 550˚C, after which the alloys are susceptible to grain boundary unpinning, phase instability and a loss in creep strength [1]. This is attributed to the coarsening of the $M_{23}C_6$ precipitates at high temperature [2].

Advanced RAFM steels, or ARAFM steels, are being developed by the UK NEURONE (NEUtron iRradiatiOn of advaNced stEels) programme to operate above 550˚C and increase the thermodynamic efficiency of the power plant [3]. The ARAFM design methodology seeks to combine an optimised alloy chemistry with refinements in the thermomechanical treatment (TMT) of the alloy to produce a microstructure strengthened by a fine dispersion of metastable, radiation-resistant MX-type precipitates.

In addition to the increased operating temperature, there is a further desire to improve the microstructural stability of RAFM steels under irradiation. Several candidate fusion powerplants, including the UK's Spherical Tokamak for Energy Production (STEP) program, are favouring a spherical tokamak geometry due to the increases in efficiency and plasma stability [4]. However, this geometry fuels a need for materials with an increased ability to retain their properties under irradiation, due to the increased neutron loading this geometry will impart [5]. It is envisioned that this fine MX precipitate dispersion will also increase the point defect sink strength of the alloy, thereby also improving resistance to radiation damage [6].

When looking at conventional RAFM steels, the two leading candidates are the European-led EUROFER-97, and the Japanese F82H [7]. Within these programs, there does not appear to be an appetite for a higher-temperature version of F82H, with research instead focussing on properties such as increased toughness [8]. The

development of high-temperature EUROFER-97 has focussed on producing a version strengthened by a fine dispersion of oxide particles (yttria), i.e. ODS-EUROFER [9]. However, these materials suffer from similar drawbacks to other ODS (oxide dispersion strengthened) steels, namely a manufacturing route limited by small quantities of mechanically alloyed powder, and reduced fracture toughness [9], [10].

Perhaps the most comparable steels to those produced within the NEURONE program are therefore those that were produced within the United States as Castable Nanostructured Alloys (CNAs). These also seek to exploit an increased density of MX precipitates to pin martensitic lath boundaries and subsequently increase the operational temperature window to c. 650˚C [11]. Six CNAs, strengthened by (V,Ta)N or TiC and/or TaC carbides were produced, all of which showed yield strengths comparable to ODS-EUROFER above 500˚C, creep resistance comparable to the 0.3% Y_2O_3 version of ODS-EUROFER, but with superior toughness to both ODS- and conventional EUROFER-97 [11]. These literature data suggest therefore that an MX-strengthened approach is a promising avenue of investigation.

However, characterising MX precipitates that have diameters below 10 nm in these newly developed materials is very challenging. Their microstructure consists of fine martensite laths containing a high dislocation density, making bright-field transmission electron microscopy (TEM) imaging difficult [12], and additionally the precipitates are often coherent and therefore do not produce any strain contrast [13]. Dark-field imaging is hampered by the inability to show all the reflections at one time [14]. Chemistry-based techniques are also difficult: STEM (scanning transmission electron microscopy) typically relies on Z- (mass) contrast, which is also minimal for VN within an iron matrix [12]. Alternatively, energy-dispersive x-ray spectroscopy (EDX)-based visualisation requires significant scanning times to generate enough signal from small precipitates. While energy-filtered transmission electron microscopy (EF-TEM) has been used [13] it required very thin samples (<20 nm) to detect the smallest MX precipitates, as well as careful analysis by skilled microscopists. There is therefore a need for a robust and rapid analysis technique for visualising and analysing MX precipitate density in this family of steels, particularly for materials development efforts where many samples are of need of characterisation.

This work therefore reports on two avenues of research: first, on the irradiation performance of an industrially-scalable ARAFM steel produced within the UK's steel supply chain that demonstrates superior performance compared to EUROFER-97. Second, a novel method based upon 4D-STEM that can be used to easily visualise the MX precipitates that provide its outstanding properties.

2. Experimental Methods

2.1. Alloy Development and Manufacture

The compositions of the two very similar ARAFM steels investigated within this work as measured by optical emission spectroscopy (OES) are detailed in Table 1. The first is a NEURONE-developed steel referred to here simply as "NEURONE ARAFM-1". The second was developed prior to the NEURONE program as part of the EUROFER Rapid Alloy Prototyping project [14], and is therefore referred to as "EUROFERAP" throughout this work. Both alloys were designed as a refinement of the EUROFER-97 chemistry, with a reduction in carbon and an increase in vanadium to favour MX precipitate formation (specifically VN). The thermomechanical treatments (TMTs) of the two alloys are similar, involving hot rolling to a reduction of approximately 50%, followed by a long hold at 900˚C – above the $M_{23}C_6$ formation temperature – to promote VN precipitation. The final step was a 750˚C and a 730˚C temper for the NEURONE ARAFM-1and the EUROFERAP alloy, respectively.

Table 1: Composition of the investigated alloys, and the average target specification for EUROFER-97, a conventional RAFM steel.

Alloy	C	Cr	Mn	Ta	V	W	N	Si
EUROFER-97	0.1	9	0.4	0.12	0.2	1.1	0.015-0.045	0.025
NEURONE ARAFM-1	0.083	8.19	0.196	0.021	0.265	2.12	0.027	0.164
EUROFERAP	0.06	8.7	0.26	0.04	0.3	2.1	0.036	0.15

2.2. Irradiation Conditions

To assess the effect of displacement damage on the microstructure and mechanical properties, self-ion irradiation was conducted at the Dalton Cumbrian Facility, UK, using 10 MeV Fe^{2+} ions at a temperature of 350 ˚C to peak doses of 1, 10, and 100 displacements per atom (dpa). The "1 dpa" samples were irradiated to a total fluence of 1.06×10^{15} ions/cm^2 over two hours, to achieve a dose ranging from 0.15 dpa at the surface to 1 dpa at the Bragg peak. The "10 dpa" and "100 dpa" samples were irradiated to a total fluence of 1.06×10^{16} and 1.06×10^{17} ions/cm^2 over fifteen and seventy hours, respectively. These correspond to dose rates of 1.4×10^{-4} , 1.8×10^{-4}, and 4.0×10^{-4} dpa/s inside the Bragg peak for the 1, 10, and 100 dpa samples, respectively. Figure 1a shows the dpa profile, generated by the SRIM software [15] using the quick Kinchen-Pease method, a displacement energy set to 40 eV [16], and lattice binding energy set to the default of 3 eV.

A single energy implantation was performed to avoid the influence of additional injected ions on the microstructure. Throughout the manuscript the samples will be referred to by these peak damage levels for simplicity. It should be noted that values from the micro-mechanical tests, e.g. indentation hardness, will be averaged over the deformation volume – typically estimated at five to ten times the indentation depth [17] – and therefore the damage profile. They will therefore necessarily include a contribution from the less-damaged material up to the Bragg peak, and thus may not be a perfect, quantitative representation of the mechanical properties that would be obtained from uniformly (e.g. neutron) irradiated material. [17]

A further proton irradiation campaign at the Dalton Cumbrian Facility was carried out to assess the threshold at which low temperature hardening embrittlement (LTHE) is prevalent. Irradiations at nominal temperatures of 250 ˚C, 350 ˚C, and 400 ˚C were performed, with an infrared camera used to capture thermal emission measurements calibrated against reference thermocouples. These additional measurements suggest the actual sample temperatures were 190 ˚C, 330 ˚C and 410 ˚C. The samples were irradiated using 2 MeV protons to a total fluence of 1.5×10^{19} ions/cm^2 over twenty-four

hours, to achieve a dose of 0.5 dpa at 30% of the Bragg peak depth (i.e. roughly in the plateau region), as shown in Figure 1b. All the irradiation conditions are summarised in Table 2.

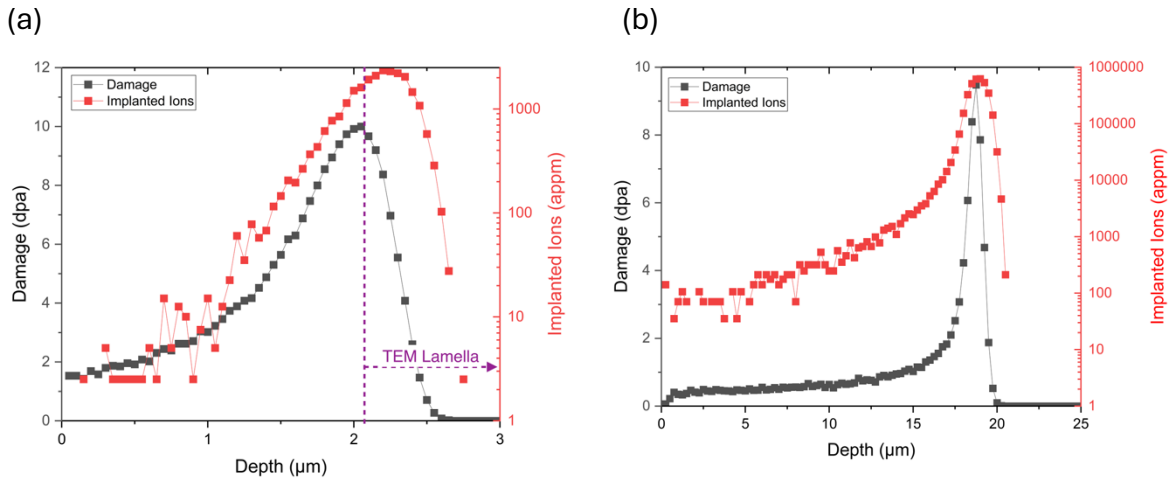

Figure 1: Damage profiles as predicted using SRIM (Stopping Range of Ions in Matter) for (a) the 10 dpa self-ion irradiation campaign (the depth profile being unchanged at other damage levels), and (b) the proton irradiation campaign. In (a) the depth from which the TEM lamella extracted from the 100 dpa sample was analysed is indicated.

Sample Shorthand	Irradiating Species	Irradiation Temp (˚C)	Irradiation Energy (MeV)	Irradiation Fluence (ions/cm^2)	Dose (dpa)	Dose Rate (dpa/s)
1 dpa	Fe^{2+}	350	10	1.06×10^{15}	1 at Bragg Peak	1.36×10^{-4}
10 dpa				1.06×10^{16}	10 at Bragg Peak	1.82×10^{-4}
100 dpa				1.06×10^{17}	100 at Bragg Peak	3.94×10^{-4}
Proton-irradiated	H^+	250	2	1.5×10^{19}	0.5 at 30% Bragg peak depth	5.78×10^{-6} at 30% Bragg peak depth
		350				
		400				

Table 2: Summary of irradiation conditions for all the materials investigated in this work.

2.3. Micromechanical Testing

Prior to irradiation, samples were prepared to a mirror polish using standard metallographic techniques, consisting of SiC grinding papers to a 2500-grit finish, followed by successive diamond polishing to a 1 μm finish. A short, ~60 second polish using colloidal silica was used as the final step, the time being restricted to avoid any preferential etching of the grain boundaries.

All nanoindentation testing was carried out on a KLA iMicro nanoindenter system, equipped with either a diamond Berkovich indenter or a diamond spherical indenter, both supplied by Synton MDP. The area functions of the indenters were determined

using indents into a fused silica calibration sample, using the typical Oliver-Pharr method in the case of the Berkovich tip [18]. A spherical tip calibration function as suggested by Leitner et al. [19] was used to determine the tip area function for the (nominally) 5 μm diameter indenter.

To assess radiation hardening, the hardness of each self-ion irradiated sample was measured using the Nanoblitz 4D test method from KLA. This performs a test using continuous stiffness measurement at a strain rate of 3 s^{-1} but with incremental millisecond pauses to measure hardness and modulus without the plasticity errors that would otherwise be present when testing at this rate [20]. Resultantly, hundreds of indents can be performed on each sample in reasonable experimental timescales. On the self-ion irradiated samples, mechanical properties of the irradiated layer were extracted between indentation depths of 200-400 nm in order to balance confining the plastic zone within the irradiated layer, and the experimental influences of surface roughness, tip blunting and the indentation size effect. In the proton irradiated samples, depths of 275-500 nm were chosen as representative of the 0.5 dpa damage levels away from significant influence of the Bragg peak. Note these depths only refer to data extracted from indents performed with a Berkovich tip.

In order to understand the deformation mechanisms within these materials, and to assess whether they are affected by radiation damage, strain rate jump tests using the method of Maier [21] were additionally performed using the Berkovich tip. Indents were performed at a strain rate of 0.2 s^{-1} to a depth of 150 nm, followed by a jump to 0.001 s^{-1} for the next 100 nm after which the rate returned to 0.2 s^{-1}. The change in hardness was analysed at this "250 nm" jump to determine the rate sensitivity. This depth was chosen to balance maintaining the plastic zone around the indenter tip within the irradiated layer with the avoidance of errors arising from surface roughness or tip calibration uncertainties.

As corroboration, a strain rate sweep test, very similar to the method introduced by Holz and Merle [22], was conducted. These tests have the advantage that the strain rate sensitivity is evaluated from a greater number of data points compared with a single jump. However, they may be more influenced by the indentation size effect. The tests were conducted at a constant strain rate of 0.2 s^{-1} until a depth of 250 nm, after which

the strain rate was ramped down to 0.01 s^{-1} over the next 150 nm to give a total indentation depth of 400 nm.

Finally, to determine an indentation stress-strain curve by which the work hardening behaviour could be assessed, spherical indents were performed at a pseudo-constant strain rate of 0.001 s^{-1}, using a load-controlled function proportional to $\frac{\dot{P}}{P^{2}/_{3}}$ as suggested by Feldner [23]. Around 64 spherical indents were performed in each case. The yield stresses and work hardening coefficients were acquired using a custom analysis script written in Python. This first performs a zero-point calibration (essentially refining the surface detection) based upon the work of Kalidindi [24], followed by a fit to a modified version of the Ramberg-Osgood equation [25], [26] that splits the measured strain into an elastic and plastic component (Equation 1). Here, ε is strain, σ the stress, E the Young's modulus, and α is the proof strain (0.2% in this work). σ_y is then the fitted yield stress, and n a parameter related to the work-hardening. A set of six exemplary curves and their associated fit are shown in Figure 2, with the yield stress shown as the dotted point. While the form of the Ramberg-Osgood equation does not allow for the capturing of strain-softening effects, the elastic, initial yield and early hardening behaviour was well-fitted.

Equation 1

$$\varepsilon = \frac{\sigma}{E} + \alpha\left(\frac{\sigma}{\sigma_y}\right)^{\frac{1}{n}}$$

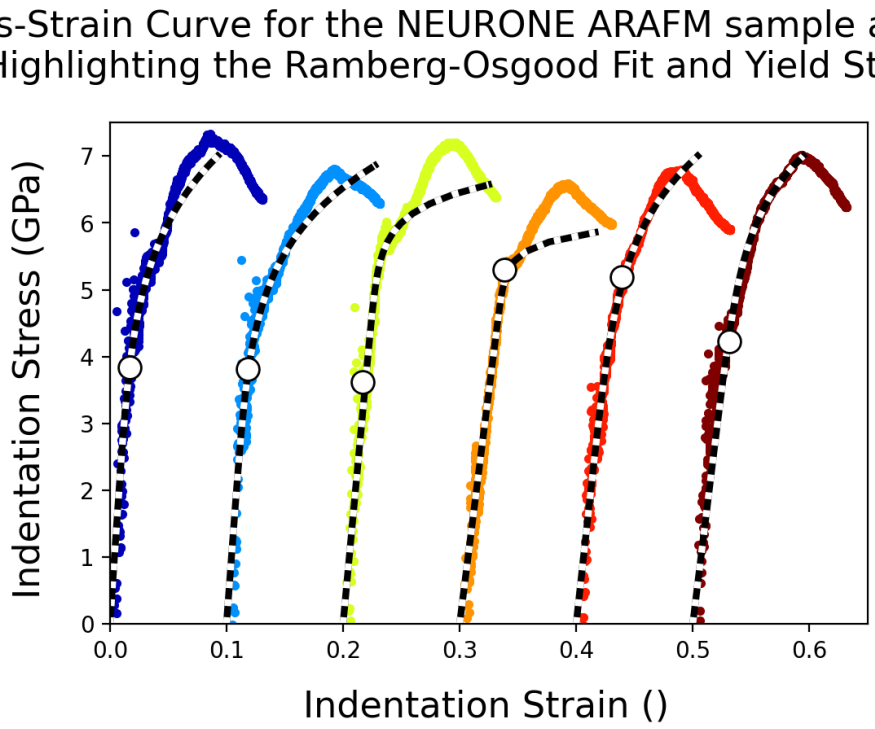

Figure 2: A set of six exemplary curves (colour) and their associated fit following the Ramberg-Osgood equation (black, dashed line). The calculated yield stress is shown by the large white circle. Each curve is offset by 0.1 strain for clarity.

To attempt to account for thermal effects such as annealing during the prolonged exposure to the ion beam, irradiation hardening for the self-ion irradiated samples was first calculated by performing testing on the irradiated section of the matchstick and subtracting the hardness determined from an area of the matchstick that was blanked by the sample holder and therefore was not exposed to the ion beam. However, it was observed these unirradiated regions do nevertheless increase in hardness with increasing dose / time. To exclude the possibility this is coming from contamination, the irradiation hardening was also calculated with respect to blanked area of the '1 dpa' sample as it is expected that in this case the contamination is minimal. These data are subsequently plotted as a 'hardening over the first sample'. For the proton irradiated sample, as the goal was to probe thermal effects, the irradiation hardening was calculated with respect to reference samples that were neither irradiated nor heated.

For all indents, regardless of method, the indent spacing was specified to be greater than ten times the ultimate indentation depth to prevent the plastic zone around each indent affecting the mechanical response of its neighbours [27].

2.4. Electron Microscopy

Scanning electron microscopy (SEM) images were acquired using a Tescan MIRA3 electron microscope at a 20 keV accelerating voltage, with electron backscatter diffraction (EBSD) collected using the attached Oxford Instruments Symmetry 2 detector.

A transmission electron microscopy (TEM) sample of the NEURONE ARAFM-1alloy irradiated to 100 dpa was produced via the focussed ion beam (FIB) lift- out method [19] across the irradiated and non-irradiated regions of the NEURONE ARAFM-1alloy, with the region localised to a single crystal of BCC iron. FIB was conducted at the Materials Research Facility (MRF) at UKAEA using a FEI Helios Nanolab 600i, with a Ga beam energy set to 30 kV for thinning the foil and 2 kV for final cleaning. TEM data were acquired using an FEI Talos with a Quantum Detectors Merlin direct electron detector. A 5 µm condenser aperture was used to create a pseudo-parallel beam with a semi angle of 0.75 mrad.

2.5. STEM Data Processing

As described earlier in this manuscript, the “advanced” versions of RAFM steels can be considered as those with a fine dispersion of MX precipitates, however these are very difficult to observe using most TEM imaging techniques. Therefore, in order to visualise these, a 4D-STEM (scanning transmission electron microscopy) dataset was acquired and processed using a novel method described here.

Two useful aggregate diffraction patterns were constructed from the 4D-STEM dataset; the average pattern and the ‘maxima’ pattern. The average pattern is simply the average of all the diffraction patterns acquired. The maxima is the maximum value of all the patterns in a given pixel.

More formally, the dataset can be described as a function of four variables α, β, x, and y. Here, α and β are the dimensions of the diffraction patterns and x and y are the dimensions of the real space image. The maxima pattern is created by finding the maximum datapoint for each fixed value of α and β, with x and y still allowed to vary (Equation 2).

Equation 2

$$\max_{x,y} = f(\alpha_i, \beta_i, x, y)$$

The average diffraction pattern (Figure 3a), can be thought of as a pseudo-SADP (selected area diffraction pattern). The matrix, which comprises the vast majority of the volume fraction of the region of material examined, dominates the diffraction pattern. The matrix pattern is therefore readily identifiable in the average pattern. The maxima pattern shows every phase that exists within the analysed volume of material, simultaneously. This is useful because it is insensitive to volume fraction and so highlights phases with very low volume fractions. Non-matrix (precipitate) reflections were identified as those present in the maxima, but not strongly present in the average pattern. Reflections were identified using the 'find maxima' function in ImageJ [28].

Within the maxima pattern (Figure 3b), bright rings around the matrix reflections can be seen. The multiple rings arise from 'double diffraction', a matrix reflection becomes sufficiently bright to cause noticeable secondary diffraction from itself. The rings are differentiated into a fine array of spots, which could be produced either from the MX precipitates, or from damage produced from the FIB preparation. To eliminate this latter possibility of amorphisation due to FIB damage, two maxima patterns were produced. One from the irradiated region and another from the non-irradiated region, these are shown in (Figure 3c) and (Figure 3d), respectively. The rings disappear in the maxima pattern from the irradiated region. As discussed more later, this demonstrates that there has been precipitate dissolution in the irradiated region and that the rings are not a result of FIB damage, as this would be expected throughout the lamella.

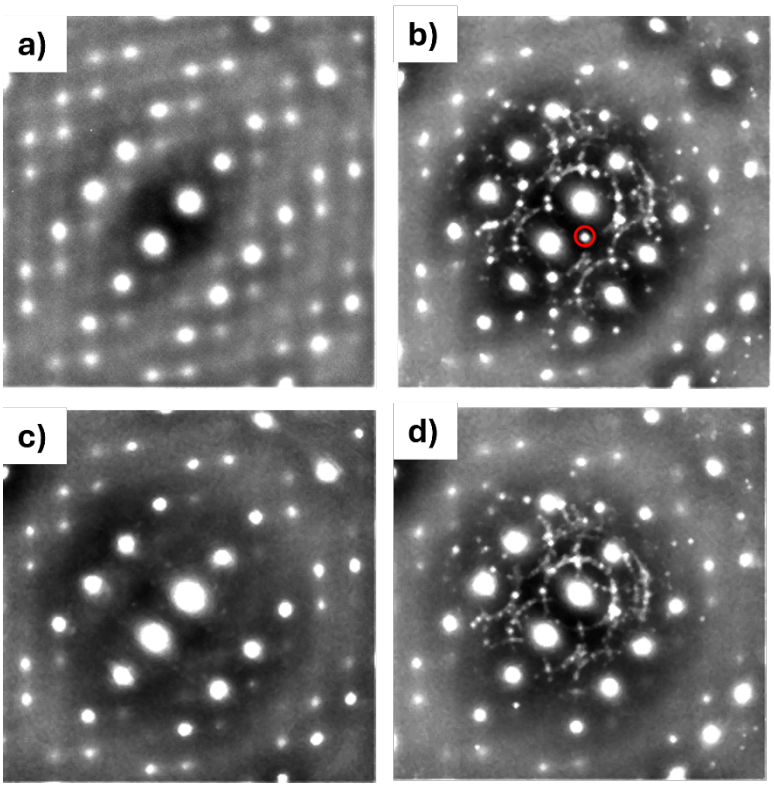

Figure 3: Diffraction patterns extracted from a 4D STEM dataset taken from a region of the material containing both irradiated (350˚C, 100 dpa) and non-irradiated material. (a) Average pattern of the whole region, encompassing both irradiated and unirradiated material, showing primarily matrix reflections from BCC Fe. The grain is orientated down the [103] zone axis. (b) Maxima pattern of the whole region, the red circle highlights the reflection used to create the images shown in Figure 5. (c) maxima pattern from the irradiated region, (d) maxima pattern from the non-irradiated region. The patterns have had their intensities normalised in order to remove saturation; dark saturation at the edges and white saturation in the middle. The intensity of the patterns centre is orders of magnitude higher than the edges.

The 4D-STEM dataset can be further processed to create 'virtual dark field' images (VDFs) that allow for precipitate visualisation. Here, two virtual apertures were placed around every non-matrix diffraction spot; a circle of radius 'r' and a ring of inner radius 'r' and outer radius '$r + 1$' where $r = 4$ pixels.

Incoherent scattering is both present at all angles in the diffraction patterns, and variable. It varies both as a function of angle, and mass-thickness of the volume of material. Conventional dark field images of weakly diffracting phases (e.g. due to size) have a high signal (phase of interest) to noise (incoherent scattering) ratio. The ring virtual aperture serves as a 'background', to approximate the incoherent scattering locally within that region. This allows for the creation of 'corrected dark field' (CDF) images where the intensity of the image, I, is given by Equation 3.

Equation 3

$$I_{corrected} = I_{circle} - I_{ring} \times \frac{Area_{circle}}{Area_{ring}}$$

3. Results

3.1. SEM Microstructural Analysis

A representative EBSD map is given in Figure 4a for the NEURONE ARAFM-1 steel. It can be seen that the microstructure is fully ferritic-martensitic, with no additional phases detected, e.g. delta-ferrite or Laves. The Matlab library MTEX was subsequently used to reconstruct the parent austenite grains from the martensitic microstructure, following the procedure of Niessen et al. [29]. Figure 4b plots the angular deviation from known austenite-martensite crystallographic relationships, such that high angles (~5˚) are indicative of prior austenite grain boundaries (PAGB). From this method, the prior austenite grain size is around 50 µm, somewhat larger than that of the 5-10 µm reported for EUROFER-97 [30][31], but not unreasonable for an engineering alloy. Overall, the thermomechanical treatments applied have been successful in achieving the desired microstructure at this scale.

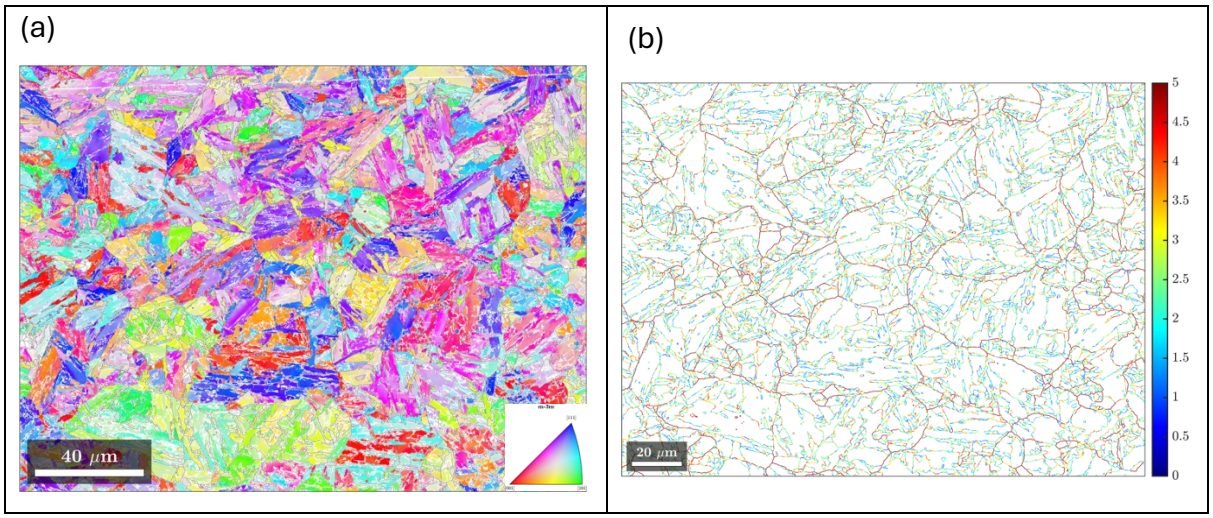

Figure 4: (a) EBSD of the NEURONE ARAFM-1 steel, indicating a fully ferritic-martensitic microstructure. The IPF is shown bottom-right. (b) The angular deviation from known austenite-martensite crystallographic relationships, such that high angles (~5˚) are indicative of prior austenite grain boundaries (PAGB).

Identifying Precipitates and Their Spatial Distribution

As mentioned, in order to visualise the MX precipitates within the steel, a 4D-STEM dataset was acquired across the irradiated and non-irradiated regions of the NEURONE ARAFM-1alloy irradiated to 100 dpa, with the region localised to a single crystal of BCC iron. Using the methodology described in section 2.4, virtual dark field and corrected dark field images were created from the 4D-STEM dataset, and are shown in Figure 5.

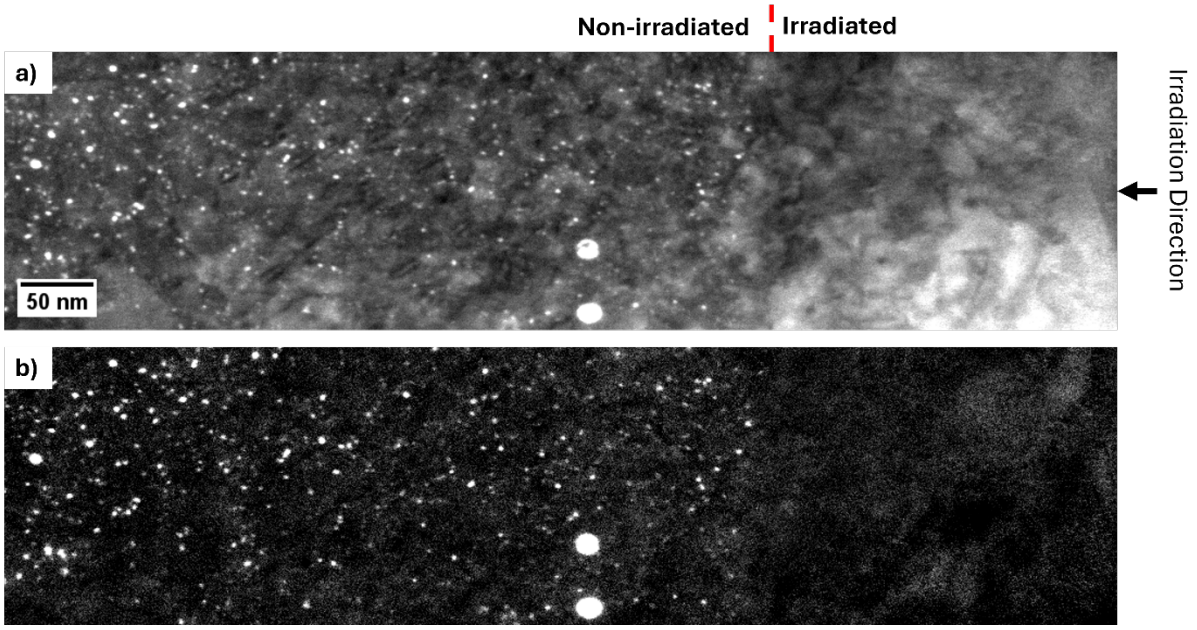

Figure 5: (a) Example of a virtual dark field (VDF) and (b) a corrected dark field (CDF) image created from the same reflection, highlighted in Figure 3b. The division between irradiated and non-irradiated shows the position after the Bragg peak, so this region will be strongly influenced by the effect of injected interstitials.

Figure 5 shows that the precipitates appear more clearly as white spots in the corrected dark field image than the equivalent virtual dark field. CDFs, individually, still retain an issue with uniform reflection brightness. The aim of this methodology is to show all precipitates in a single image to allow for a comparison between precipitate size and density in the irradiated and non-irradiated regions. Consider an ideal scenario, where the precipitates have an identical orientation relationship with the matrix, such that within a single grain of the matrix, all precipitates have the same zone axis. Subtle changes in the orientations of the matrix, on the order of milliradians, are easily caused by dislocations and can change the intensity of a given reflection significantly.

Therefore, no single CDF image is representative of the entire distribution of precipitates.

The solution to this is the same as the solution to identifying diffraction spots, discussed at the start of this section. The CDFs are a 3D (rather than 4D) dataset represented as a stack of images, from which, the average CDF image (aCDF) and maxima CDF image (mCDF) can be taken. The mCDF, shown in Figure 6 is very effective at highlighting all the precipitates simultaneously. The mCDF is bright if, and only if, a region of the diffraction pattern has a local intensity higher than its surroundings that does not arise from the matrix.

This maxima corrected dark field image therefore allows two key conclusions: first, that the MX precipitates in the unirradiated region are present at an extremely high density (c. 5×10^{22} m^{-3}, based on a lamella thickness of around 130 nm, as determined by EELS). Second, it reinforces the conclusion drawn from Figure 3c and d; the precipitates are not present in the highly irradiated, Bragg peak region. A third, tentative conclusion is also possible from the slight contrast still present in the top-right corner of Figure 6b: that some precipitates will be retained up to approximately 25 dpa. However, due to the contributions that dose rate and the presence of self-interstitial atoms have on precipitate dissolution, this cannot be stated conclusively.

While TEM analysis has only been carried out on the 100 dpa sample, there is increasing evidence in the literature that these MX precipitates are stable until several tens of (matrix) displacements per atom. In addition to the previous study on a very similar ARAFM [14] where precipitates were re-dissolved past 40 dpa, Tanigawa et al. saw TaC dissolution past 20 dpa at 500 °C [32] while Kano et al. report TaC stability to 50 dpa at 400 °C [33]. Tan et al. investigated a variety of MX chemistries, but in general saw MX stability to 49 dpa at 500 °C [34]. Green saw TiC dissolution at 15 dpa for irradiation temperatures <400 °C, and dissolution at 50 dpa at all temperatures. All these works were performed using ion-irradiation, hence the dose rates should all be relatively comparable.

Therefore, it is strongly suspected that the MX precipitates are retained in the other samples (1 and 10 dpa self-ion irradiated samples, as well as the 0.5 dpa proton

irradiated materials) as the damage levels are significantly below the thresholds reported in the literature.

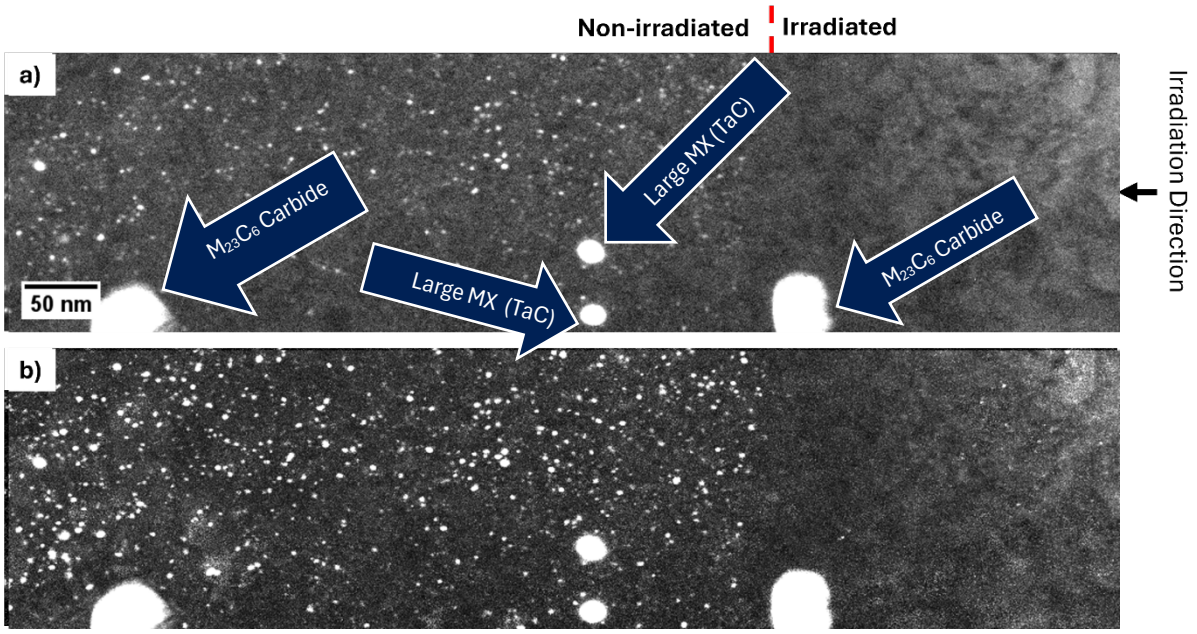

Figure 6: a) Average corrected dark field (aCDF) and (b) Maxima corrected dark field (mCDF) images of the 100 dpa NEURONE ARAFM-1 sample. As described, the mCDF can be taken as a visualisation of all the precipitates present in the lamella. Here too the division between irradiated and non-irradiated shows the position after the Bragg peak, so this region will be strongly influenced by the effect of injected interstitials. Two large $M_{23}C_6$ carbides (identified via their diffraction pattern) are visible towards the bottom of the image (labelled in (a)), as well as a pair of larger MX precipitates in the centre, likely TaC based upon Ta enrichment visible in EDX mapping. The right-hand edge of the image is 2.1 µm below the surface of the sample.

3.2. Irradiation Hardening

The unirradiated hardness of the NEURONE ARAFM-1 alloy, as determined from indents performed in the unimplanted (but still heated) ends of the 1 and 10 dpa samples is 4.66 ± 0.38 GPa. The unimplanted hardness for each sample and the hardnesses in the irradiated are shown in Figure 7, which plots the hardness after irradiation for the NEURONE ARAFM-1 samples after their respective self-ion irradiations, along with the EUROFERAP alloy after proton irradiation at the matching 350˚C irradiation temperature (exploring LTHE effects). The two datapoints corresponding to the 100 dpa sample come from two arrays of indents spaced some millimetres apart in the sample to verify the performance was not due to experimental error or sample inhomogeneity.

The difference in hardness in the EUROFERAP and ARAFM-1 materials is likely a strain rate effect, as they were indented at 0.2 s^{-1} and 3 s^{-1}, respectively.

The data expressed as a percentage increase over the base value are displayed in Figure 8, which also contains several datapoints from the literature for comparison, shown as orange diamonds, mostly consisting of hardening of EUROFER-97 as measured from nanoindenation after ion irradiation [35][36][37] with one point taken as an increase in yield stress after neutron irradiation [2]. This figure plots two different methods of calculating hardness: solid points labelled “Same Sample” are calculated comparing the irradiated and unirradiated areas of each sample such that thermal effects are included. Open symbols, labelled “Hardening over 1st sample” are calculated as the hardness of the irradiated material over the unirradiated region of the 1 dpa sample.

When calculating hardening on a per-sample basis, i.e. the “same sample” dataset, it can be seen that very little hardening takes place at 1 dpa. At 10 dpa around a 20% hardness was measured, with no further evolution within experimental uncertainty up to 100 dpa. While a saturation in hardening is often observed around 10 dpa in RAFM steels [2] this low degree of hardening is noticeably different from the literature data (orange).

However, the 100 dpa datapoints in particular are rather divergent when hardening is calculated when compared to the 1dpa unirradiated material (open symbols). Here the hardening then rises to closer to 90%. This difference is driven by an increase in the unirradiated hardness with “damage”: from 4.4 GPa in the 1dpa sample, 5.0 GPa in the 10 dpa sample, and up to 7.3 GPa at 100 dpa. The four arrays contain almost 450 indents between them, and are made in two distinct areas for each unirradiated and irradiated region. It is therefore unlikely to be experimental error leading to the higher unirradiated values of hardness.

We suspect therefore that some contamination has occurred from the sample holder resulting in a hardened surface layer even in areas not exposed to the ion beam. As such, the open-symbolled “hardening over 1st sample” data are likely to be more representative of the true material response, given microstructural aging effects should

be limited over these temperatures and timescales (5 days at 350˚C). The discussion will therefore proceed assuming these data are the "true" results, but the others are still plotted for the sake of scientific completeness.

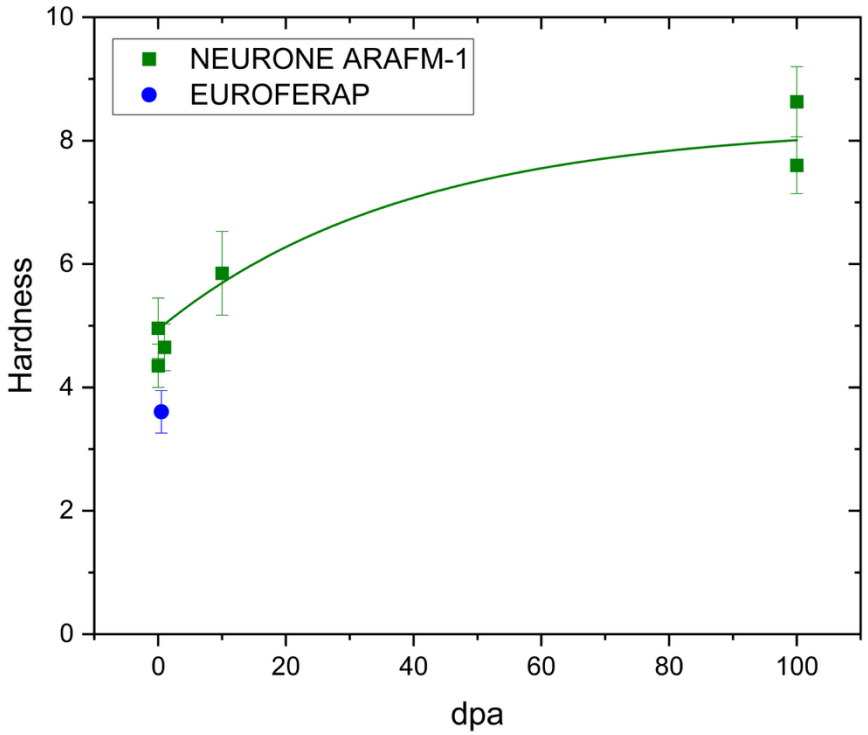

Figure 7: Hardeness as determined by nanoindentation for the NEURONE ARAFM-1and EUROFERAP samples irradiated at 350˚C. Error bars show plus / minus one standard deviation in each direction based upon the distribution of hardness.

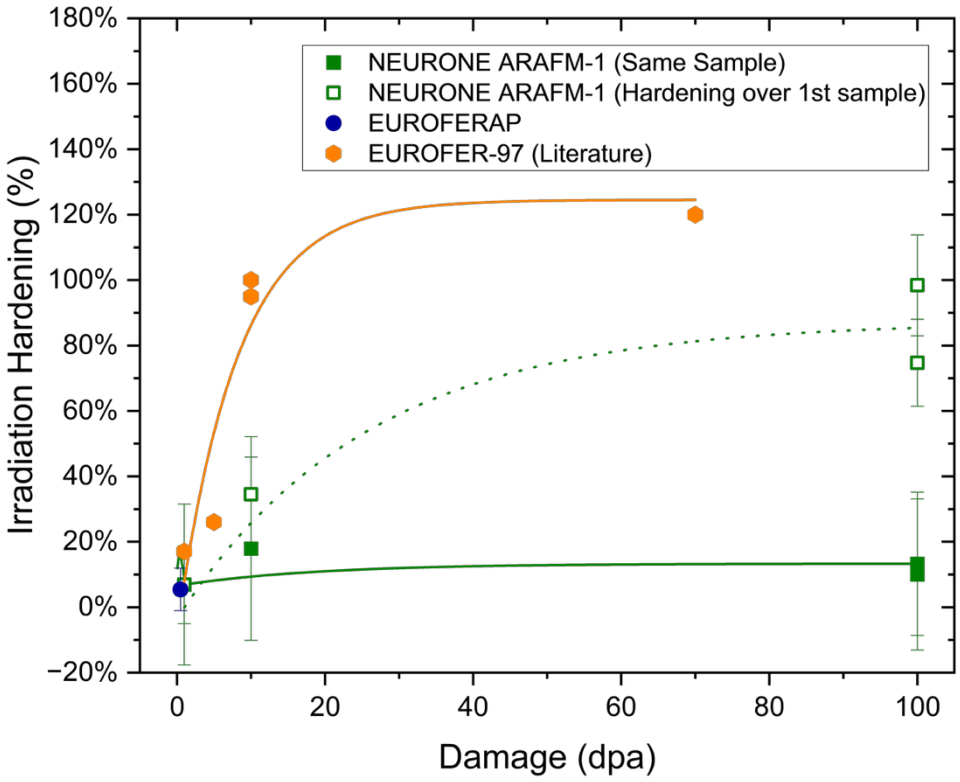

Figure 8: Irradiation hardening expressed as a percentage increase over the relevant unirradiated material, in order to allow comparison with the literature data [2] [35][36][37] (orange). Literature data are largely taken from ion-irradiation campaigns on EUROFER-97, with properties also measured via nanoindentation. Two methods of calculating hardening are shown: "Same Sample" data are taken from unirradiated and irradiated sections of the same sample for each irradiation condition, i.e. including thermal effects. "Hardening over 1st sample" data are caluclated with respect to the unirradiated region of the 1 dpa sample in an effort to exclude potential contamination effects. It should be noted that as this is a plot of hardening, as opposed to hardness, that these uncertainties are the root-square sum of the standard deviations of the irradiated and unirradiated material, and hence are larger than the "normal" spread for a single dataset.

3.3. Variable Strain-Rate Indentation

The activation volumes as determined by strain rate jump (SRJ) testing and the strain rate sweep (SRSweep) method are given in Figure 9, calculated using a Burgers vector length of 0.25 nm [38]. While noisy, the activation volumes determined by both methodologies are similar in terms of the deformation mechanism they imply, and the average value of 34 b^3 in the unirradiated condition is consistent with values found in the literature [39]. This value is consistent with the expected behaviour for iron at room temperature, indicating deformation controlled by the glide of screw dislocations pinned largely by the Peierls stress. It can also be seen that this value does not change even after irradiation to 100 dpa (29 b^3 when averaged).

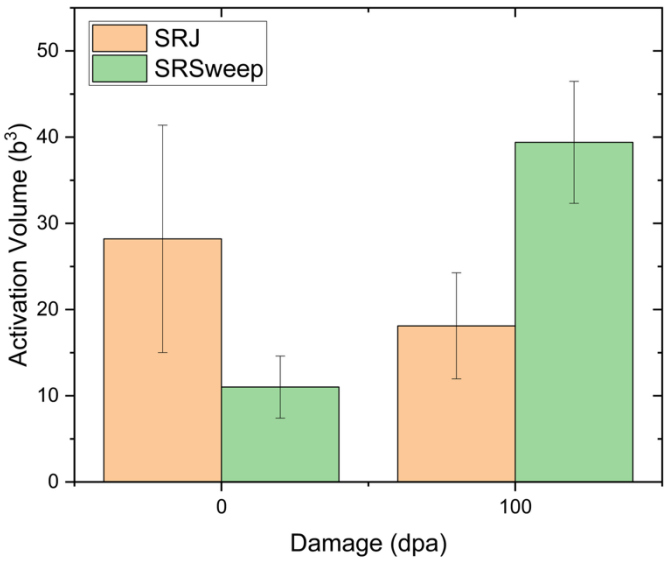

Figure 9: Activation volumes as determined by strain-rate jump (SRJ) and strain rate sweep testing in the unirradiated and irradiated sections of the sample irradiated to 100 dpa, such that any thermal effects are comparable.

3.4. Spherical Nanoindentation Curves

A nominally 5 μm spherical indenter was used to generate stress-strain curves for the NEURONE ARAFM-1samples to allow for comparison between pre- and post-irradiation work hardening behaviour. The curves from the c. 40 indents performed in each of the unirradiated and irradiated portions of the 100 dpa NEURONE ARAFM-1sample are shown in Figure 10, along with curves from material irradiated to 10 dpa .

While strain is calculated, it is not plotted except in Figure 10d as plotting against indentation depth allows for a better comparison with respect to the depth of the ion irradiated layer. Two facts should be noted regarding the stress axis: firstly the stress is simply calculated as the force divided by the indentation contact area. This is because the strain-dependent constraint factors such as those from Leitner [19] that could be used to accurately convert to a representative uniaxial stress have not been validated on the ferritic-martensitic microstructures investigated here. Secondly, the data are subject to an indentation size effect, where the increased density of geometrically necessary dislocations lead to higher stresses being measured compared to macroscopic tests [40]. Care must therefore be taken if attempting to quantitively compare these data with macroscopic curves, not only for these reasons but also the significant difference in stress state between indentation experiments and tensile testing.

It can be seen that there is largely no change between 0 (Figure 10a) and 10 dpa (Figure 10b), with both the yield stress and post-yield work hardening largely unaffected by the irradiation. After 100 dpa (Figure 10c), the yield stress has increased from 3.5 to 4.5 GPa (i.e. 30%), and strain softening is observed after ~225 nm or ~8% strain. Finally, Figure 10d plots an exemplary stress-strain curve from each of the samples in (a)-(c) to highlight better this change in yield stress and softening exhibited in the 100 dpa sample.

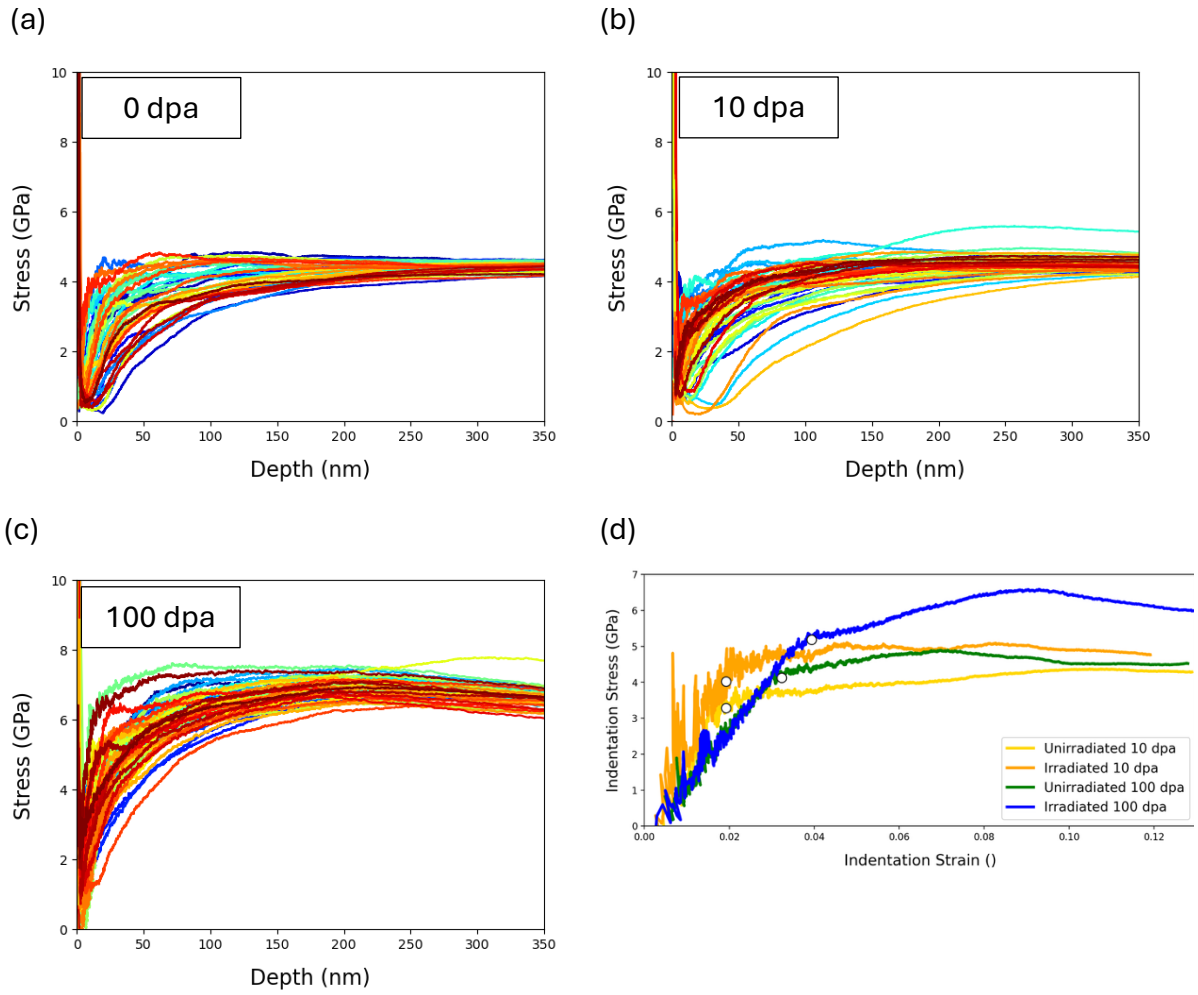

Figure 10: Stress vs indentation depth curves for the (a) unirradiated, (b) 10 dpa irradiated, and (c) 100 dpa irradiated material. The curves are plotted against indentation depth to better allow for comparison between penetration depth and the depth of the implanted layer. In (d), a single curve from each sample are plotted in terms of both stress and strain are plotted in a comparison between both the unirradiated and irradiated portions of the 10 dpa and 100 dpa samples.

Figure 11 plots the data determined as a result of fitting the Ramberg-Osgood equation to the calculated stress-strain data: (a) plots the increase in the yield stress with damage, and (b) the calculated work hardening coefficient. By-and-large the changes in yield stress (Figure 11a) match those seen from the Berkovich indentation trends (Figure 7). As noted previously, the form of the Ramberg-Osgood equation does not allow for the capturing of strain-softening effects, hence the fit and the determined work-hardening coefficients (Figure 11b) only captures the early hardening behaviour. Nevertheless, as the softening is only seen past ~8% strain, this coefficient is still a useful indicator of in-service behaviour. Therefore, it is reassuring to see that there is no

change – within experimental uncertainty – from the unirradiated value (0.083 on average) to 100 dpa (0.12).

(a) (b)

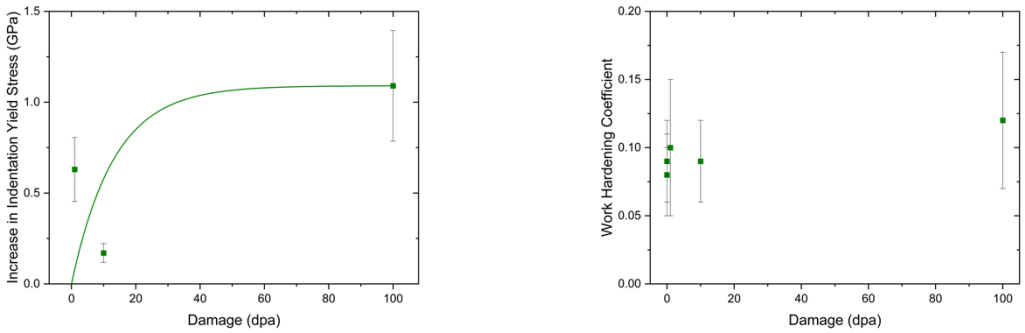

Figure 11: Spherical nanoindentation results showing (a) the increase in indentation yield stress from irradiation damage, and (b) the change in the work hardening coefficient. The line of best fit in (a) is fit to √dpa to capture the saturation in irradiation hardening seen in RAFM steels with dose [2].

3.5. Proton Irradiation: Effect of Temperature

The NEURONE ARAFM-1alloy was not subjected to proton irradiation as it all had been consumed by the time the campaign was scheduled. However, the very similar EUROFERAP alloy (detailed in Table 1) allows for a reasonable assessment of how the low temperature hardening embrittlement (LTHE) threshold might be expected to have evolved as a result of the increased strengthening. In Figure 12 the increase in hardness over an unirradiated, unheated sample is plotted for the EUROFERAP material, alongside literature data for EUROFER-97 [41] for comparison. The three proton-irradiated EUROFERAP samples were all irradiated to around 0.5 dpa of damage in the plateau region, hence the reduction in irradiation hardening with temperature is simply a result of the changing irradiation microstructure. The negligible hardening of EUROFER-97 at 400˚C results in the oft-quoted 350-400˚C limit for LTHE. It can be seen that the hardening of the EUROFERAP sample at 400˚C is only slightly above zero, given the scatter in the data, and hence it can be concluded that the LTHE threshold has only crept up <50˚C in the ARAFM, to around 400˚C.

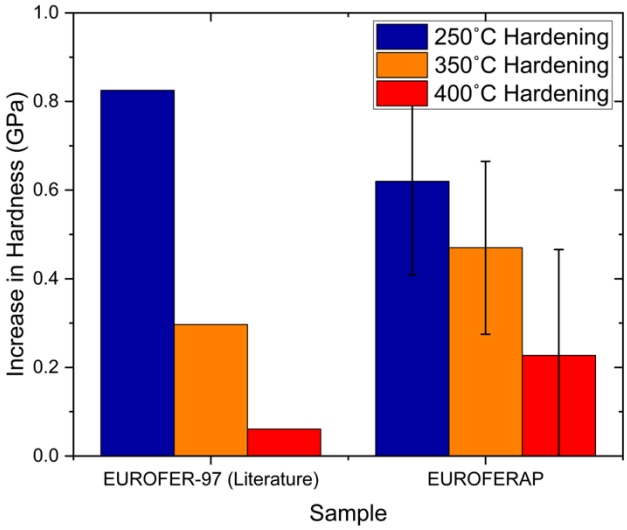

Figure 12: Hardening in the EUROFERAP samples after irradiation to 0.5 dpa with protons at varying temperatures with respect to an unimplanted, unheated sample. Data for EUROFER-97 taken from microindentation data on neutron-irradiated material from Sacksteder et al [41] .

4. Discussion

In the processing of steels, particularly RAFM steels, the thermomechanical treatments (TMTs) affect the precipitate distribution and chemistry, as well as the overall alloy microstructure [42], [43]. The alloy must undergo several phase transformations during processing; from liquid, through the undesirable delta ferrite region, into austenite for mechanical processing; cooling through alpha ferrite to room temperature to form martensite, before final tempering to transform the metastable martensite into stable ferrite. In the austenite region, TMTs are applied to reduce the cast billet into its final plate dimensions, and the microstructure is refined as the prior austenite grain (PAG) size will affect the final microstructure upon transformation to martensite [44]. As all these phase boundaries are affected by composition, and particularly in the case of highly-alloyed steels working at the edge of the austenite phase field, it is necessary to alter the processing temperatures upon refinements of the alloy chemistry.

It can be seen in the EBSD map of the sample (Figure 4a) that the updated (proprietary) TMTs for this alloy have been successful: the microstructure consists of fine

martensitic laths and there is no evidence of any retained delta ferrite. Reconstructing the PAG size shows that this alloy has an average grain size of around 50 μm.

More detailed microstructural characterisation by TEM to observe the precipitate microstructure (Figure 6b), revealed a fine, dense dispersion of MX precipitates, very likely VN precipitates, with a volumetric density of 5×10^{22} m^{-3} . Prior characterisation of a similar ARAFM steel [14] determined a number density for the precipitates of ~1×10^{22} m^{-3}, with the needles having a mean length of ~16 nm, and mean width ~5 nm.

It likely the combination of both the fine microstructure and the high precipitate density that leads to the high sink strength required for radiation-resistant microstructures [45]. This is evidenced in Figure 7 and Figure 8 where the extremely low levels of radiation hardening can be seen: 35% at 10 dpa where EUROFER-97 exhibits a near-doubling of its hardness. A more subtle, but non-zero improvement is still seen at 100 dpa once the MX precipitates have dissolved: 85% harder compared to the 120% of EUROFER-97.

While the MX precipitates acting as efficient defect recombination centres likely explains the low hardening at 10 dpa, the result at 100 dpa cannot be attributed to the precipitate density. In both Figure 6b, as well as a study on a similar VN-strengthened ARAFM [14], there is complete dissolution of the precipitates at damage levels >40 dpa. The high density of grain boundaries, as well as the pre-existing dislocation density, are therefore also likely significant contributors. While the dislocation density has not been characterised in this work, EUROFER-97 with a similar final tempering temperature exhibits a high dislocation density in the martensite laths of 9.0×10^{13} m^{-2} [46].

It is therefore most likely that two deformation mechanisms are occurring as irradiation proceeds. The mechanical response is dominated by radiation hardening on top of precipitate strengthening up to around 10 dpa, where based on literature trends [2], it likely saturates. Precipitate dissolution past ~40 dpa [14] would likely lead to the alloy softening, however this is compensated for by additional radiation hardening, resulting in a net hardening of 85% at 100 dpa. Nevertheless, a comparison with literature data on EUROFER-97 is very favourable, particularly at 10 dpa where Gaganidze [35] shows an increase in yield stress from 550 MPa in the unirradiated condition to 1075 MPa at 300 ˚C (a 95% increase) and 1200 MPa after 70 dpa at 332 ˚C (a 120% increase).

Bhattacharya's review shows that most RAFM steels show similar increases in yield stress [47]. The lower dose rates of neutron irradiation are expected to cause increased hardening effects with respect to the self-ion and proton irradiations performed here [48]. Nevertheless, comparisons with self-ion irradiated EUROFER-97 in the literature from Heintze [49] (26% increase at 5 dpa) and Das [37] (a 17% increase at 1 dpa) are still favourable, with the NEURONE ARAFM-1 alloy showing reduced irradiation hardening, circa 30%, in the 1-10 dpa range where MX precipitates are present.

Although the fine precipitate distribution contributes to the radiation hardening resistance of this new alloy, their instability under irradiation may be problematic in breeder blanket applications if their presence is a significant contributor to the strength of the alloy, and hence a weakening of the alloy would occur upon their dissolution. In terms of assessing strength, a dispersed barrier hardening model can be applied to estimate the contribution of the precipitates to the overall strength of the alloy. The model states that the increase in strength is given by Equation 4 [50]:

Equation 4

$$\sigma = M\ \alpha\ \mu\ b\ \sqrt{N\ d}$$

With appropriate values of M of 3.06, μ of 75.3GPa, and b of 0.249 nm, taken from literature values for irradiated stainless steels [50]. A value of α = 0.33 [51] is assumed due to the relatively small size of the precipitates, thus assuming they are relatively weak obstacles. Finally, the precipitate density was calculated to be N = 5.0×10^{22} m^{-3}, and their size (d) can be crudely estimated as the average of their length (16 nm) and width (5 nm), assuming that dislocations will encounter them from both directions [14].

Using these parameters, the estimated increase in strength from the MX precipitates is evaluated at 430 MPa, equivalent to a 1.3 GPa increase in hardness when converting from yield strength to hardness using the Tabor relationship [52]. This 1.3 GPa is around 30% of the total measured hardness of the as-received, unirradiated materials, i.e. it is a rather significant fraction. In comparison, for EUROFER-97, a total MX (TaC + VN) precipitate density of 1.45×10^{20} m^{-3} with an average size of ~ 50 nm has been reported [30]. Using the above parameters, this corresponds to an estimated increase in

strength of 51 MPa, i.e. around 10% of that of the NEURONE ARAFM-1 steel, and also only a tenth of EUROFER-97's room-temperature strength.

The dissolution of the precipitates is compensated for by increased levels of radiation hardening, i.e. the material does not soften up to end-of-life levels of damage (Figure 8). However, it is therefore necessary to search for any other changes in mechanical properties that may occur as a result of the MX dissolution, given their significant contributor to overall strength.

A further insight into the deformation mechanisms within the material can be gained using nanoindentation strain rate jump tests [21] and strain rate sweep tests [22]. These were performed to determine the rate-controlling step of dislocation mobility, and show (Figure 9) that in all conditions, the activation volumes of a few tens of cubic Burgers vectors are indicative of (screw) dislocation mobility controlling plasticity [53]. That mobility is not controlled by Orowan bowing around precipitates is likely the reason why the mechanism is unchanged after even 100 dpa of damage. Screw dislocations controlling plasticity is not unexpected for a body-centred cubic metal below its critical temperature; the same result is observed in neutron-irradiated tungsten in both the unirradiated and irradiated condition [54]. It should be noted that in the work on tungsten [54] , a significant shift in the brittle to ductile transition temperature was still observed, attributed to a decrease in average dislocation velocity. It is therefore emphasised that these results on this ARAFM steel cannot be taken to conclude that its toughness or its BDTT is unaffected by radiation damage.

As an intermediate conclusion therefore, the very high density of MX precipitates contributes significantly to the overall radiation hardening resistance of the new ARAFM steel by acting as extremely potent defect sinks. While a significant factor in the strength of the alloy, they do not control the onset of plasticity, and their dissolution is compensated for by radiation hardening, implying that the end-of-life strength of this alloy should not significantly degrade through the loss of the VN precipitates.

It should be noted that for the dissolution observed here, as well as in similar studies [31], [32], [34], the driving force for the dissolution is a ballistic one as a result of the heavy ion irradiation. The dose rates in such irradiations are around 10^3 - 10^4 times

faster than those that are expected to be experienced in service [48] . Therefore, it is expected that these ion irradiation studies result in increased precipitate dissolution. At first glance this is therefore a best-case scenario; the ARAFM appears to not be significantly degraded even with the worst precipitate loss possible (Figure 8).

However, the ultimate destination of the solutes must be considered. The increased levels of solid solution strengthening from 0.265 wt% V are limited: around 130 MPa [55], i.e. roughly a third of the MX strengthening. However, if there is not a strong driving force for re-precipitation, these solutes have the potential to diffuse to microstructural features such as grain boundaries where they may contribute to larger, more incoherent, and therefore embrittling second phases. This phenomenon is unlikely to be seen during experiments such as these as the timescales, and therefore diffusion distances for vacancy-mediated diffusion are limited. The dose rate thresholds for precipitate dissolution would therefore be important to elucidate in future experiments. It would also be valuable to assess of microstructural changes after long-term ageing of heavily-irradiated samples at modest temperatures (i.e. operational temperatures of 600˚C-650˚C, as opposed to 750˚C tempering temperatures) to assess whether re-precipitation occurs.

It has been suggested that future fusion alloys should be designed with as large a gap as possible between the yield stress and the ultimate tensile stress [2]. This maximising of the work hardenability of the alloy minimises susceptibility to low temperature hardening embrittlement [2]. The strain underneath a standard, self-similar Berkovich indenter is constant, typically taken as 7% [56] . Further nanoindentation tests employing a spherical tip were carried out so as to generate an (indentation) stress-strain curve and determine a work hardening coefficient in the thin damaged layer.

The trends in yield stresses and their increases after irradiation shown in Figure 11a match reasonably well with those seen in the indentation hardness data, suggesting the Ramberg-Osgood fitting carried out as part of the data analysis is performing well (Figure 2). The fits suggest that this alloy has a work hardening coefficient of around 0.1 (Figure 11b) in all conditions, even after irradiation. At first glance, this suggests that the work hardening and toughening behaviour of the alloy is unchanged.

However, it must be emphasised that this work hardening coefficient has been determined via a compressive indentation test. Therefore, care must be taken with its application. It has been shown that in unirradiated 304 stainless steel that while the work hardening coefficient determined through spherical nanoindentation is comparable to that determined through micro-tensile testing [57], the same study showed that after 10 dpa of proton irradiation, spherical nanoindentation demonstrated a significantly higher work hardening exponent than the tensile tests. This was attributed to strain localisation taking place in the tensile tests that does not take place in indentation. This is due to a combination of the compressive stress state, as well as the expanding plastic zone deforming "fresh" material throughout the course of the experiment. This is also likely the reason why a true UTS is not reached and the typical observation from Considère's criterion [58] – that the work-hardening coefficient is approximately comparable to the plastic strain at maximum stress on the stress-strain curve – is also not seen.

Interestingly, in this work, the stress-depth curves in Figure 10 do appear to show some strain softening that would be indicative of strain localisation. After approximately 200 nm in the 100 dpa material there is a small degree of softening that is not present in the unirradiated curves, nor at 10 dpa. At these shallow depths, and given the softening is not seen after 10 dpa of damage, it is unlikely that this is simply a substrate effect where softening is observed due to the stress field penetrating into the unimplanted substrate. It is not immediately obvious as to why softening is occurring here but was not observed in the literature [57]. One possible explanation is the increased damage level in this work: 100 dpa here compared with 10 dpa in the literature, leading to an increased dislocation loop density and therefore a greater degree of softening once a defect-free channel is formed.

That the work hardening coefficient does not vary after irradiation is interesting, as spherical nanoindentation tests in a series of Fe-Cr alloys irradiated up to 0.1 dpa showed in all materials a reduction in the work hardening exponent [59] with increasing damage. There are two potential explanations for this difference. The first, that the damage levels investigated here are too high to observe a decrease in work hardening rate, and it has simply saturated by 1dpa. However, in this case, it would be expected

717 that at least the work hardening rate of the as-received material would be higher. The
718 second possibility of an intrinsically lower work hardening rate in the NEURONE
719 ARAFM-1 alloy compared to binary Fe-Cr seems therefore more likely.

720 This is supported by tensile testing of similar bulk materials. As above, the room-
721 temperature yield strength of an Fe-9Cr alloy with a ferritic-bainitic microstructure is of
722 the order of 300 MPa [60], with a UTS of around 400 MPa (i.e. 33% higher). The yield
723 strength of EUROFER-97 is 531 MPa [61] with a UTS of 654 MPa (23% higher). Therefore,
724 a combination of the ferritic-martensitic microstructure, as well as the precipitate
725 strengthening, has reduced the work hardening capacity of the alloy.

726 The indentation hardnesses measured here in the as-received conditions for both
727 alloys are similar, when strain-rate effects are considered: EUROFERAP ~3.1 GPa and
728 the NEURONE ARAFM-1 ~4.6 GPa. Heinze report a hardness of 3.8 GPa for EUROFER-
729 97 at a similar indentation depth [49] as reported here. It is therefore likely that the
730 work hardening characteristics of EUROFER and these advanced RAFMs are also
731 comparable: as above, the representative strain in these tests is around 7%, and
732 therefore the indentation hardness captures the work hardening of the material
733 alongside the yield stress. The lower, and constant, values of the work hardening
734 coefficient are therefore likely to be “real”, as opposed to resulting from fitting errors.
735 There is thus tentative evidence that work hardenability of this alloy does not
736 significantly deteriorate during irradiation, further suggesting it as a promising
737 structural blanket material for future fusion power plants.

738 The final assessment for candidate structural materials is their operating temperature
739 window. There would be many candidate materials for 650 ˚C coolant outlet
740 temperatures if ductility at low temperatures were not a concern. However,
741 maintenance schedules (potentially around 40% of the plant lifetime [62]), mean that
742 power plants will spend significant amounts of time at room temperature and therefore
743 maintaining a BDTT below room temperature is therefore highly desirable.

744 Proton irradiation to a constant damage level of around 0.5 dpa but at varying
745 temperatures shows modest but measureable hardening of 20% in the EUROFERAP
746 alloy at 190 ˚C (measured irradiation temperature) / 250 ˚C (nominal irradiation

747 temperature). This persists at 330˚C (measured) / 350˚C (nominal), with an increase of
748 15% compared with as-received material. At 410˚C / 400˚C, hardening could be
749 considered to neglible considering experimental scatter (Figure 12), but is likely still
750 present at low levels. In comparison, literature data for EUROFER-97 [38] shows a
751 similar level of hardening at 250˚C and 350˚C, but the materials is clearly unchanged
752 by the irradiation at 400˚C. The low temperature hardening embrittlement (LTHE)
753 threshold for EUROFER-97 would therefore be ~350˚C, matching the operating
754 temperature windows in the literature [63]. As the EUROFERAP alloy still shows some
755 hardening after irradiation at 410˚C, it can be concluded that the LTHE threshold and
756 thus the lower operating temperature has crept up slightly to ~400˚C. It is hoped that
757 this small increase is compensated for by significant improvements in creep
758 resistance, however this remains to be shown in future work.

759 It may also be the case that using ion-irradiation to assess LTHE results in a worst-case
760 estimate of the threshold temperature. The authors are unable to find any studies that
761 use proton-irradiation or heavy-ion irradiation to assess the LTHE threshold in
762 EUROFER-97. However, a self-ion implantation study of hardening with temperature of
763 binary Fe-Cr alloys [48], including Fe-10Cr as the closest in composition to EUROFER-
764 97, still shows hardening after irradiation 400˚C with neglible hardening only seen for
765 500˚C irradiations. Thus there is a hint that the LTHE threshold is slightly overestimated
766 when using heavy ions. While this is promising for the work reported here, it is not
767 possbile to state conclusively given the differences in materials as well as irradiation
768 conditions, but would make for an interesting avenue for future studies.

769

5. Conclusions

An advanced reduced-activation ferritic-martensitic steel has been developed with superior radiation hardening resistance with respect to the EUROFER-97 upon which it was based. Through the use of novel processing of a 4D-STEM dataset, it was possible to visualise all the fine MX precipitates that led to this outstanding hardening resistance and determine a precipitate density of 5×10^{22} m^{-3}.

Self-ion irradiation campaigns up to 100 dpa at 350 °C have been performed, after which an increase in hardness of only 35% at 10 dpa was measured, where EUROFER-97 exhibits a near-doubling of its hardness. A more subtle, but non-zero improvement is still seen at 100 dpa once the MX precipitates have dissolved: 85% harder compared to the 120% of EUROFER-97. The work hardening response, as determined from spherical nanoindentation, was unchanged between the as-received state and irradiation to 100 dpa, implying that the alloy should retain modest ductility under these conditions. However, it is emphasised that resistance to irradiation hardening is only one factor in the suite of properties that structural fusion materials require, and changes in e.g. BDTT must still be assessed.

Proton irradiations at 250 °C, 350 °C, and 400 °C demonstrated that the low temperature hardening embrittlement threshold is largely unaffected, increasing by only ~50 °C with respect to EUROFER-97. A refinement of alloy chemistry and a subsequent modification of the thermomechanical treatments to favour MX precipitates is therefore a very promising strategy for the further development of fusion steels.

6. Acknowledgements

This work has been funded by the NEUtron iRradiatiOn of advaNced stEels (NEURONE) programme via Fusion Futures. As announced by the UK Government in October 2023, Fusion Futures aims to provide holistic support for the development of the fusion sector. The research used UKAEA's Materials Research Facility, which has been funded by and is part of the UK's National Nuclear User Facility and Henry Royce Institute for Advanced Materials. The alloys used in this study were developed with support from the

Research Wales Innovation Fund Collaboration Booster 2021, PROJECT #FF2. We acknowledge the support of The University of Manchester's Dalton Cumbrian Facility (DCF), a partner in the National Nuclear User Facility, the EPSRC UK National Ion Beam Centre and the Henry Royce Institute. We recognise Samir de Moraes Shubeita for their assistance during the irradiation.

7. CRediT Author Statement

James S.K-L. Gibson: Conceptualisation, Formal Analysis, Investigation, Validation, Writing – Original Draft

Alex Carruthers: Methodology, Formal Analysis, Investigation, Writing – Original Draft

Benjamin R. S. Evans: Software, Investigation

Jack Haley: Investigation

Slava Kuksenko: Investigation

Kay Song: Software

Luke Hewitt: Software

Stephen Jones: Resources

Shahin Mehraban - Investigation, resources, supervision, project administration, funding acquisition

Nicholas Lavery: Resources

David Bowden: Supervision, Funding Acquisition, Resources

8. Declaration of competing interest

The authors declare that they have no known competing financial interests or personal relationships that would influence the work reported here in this paper.

9. Bibliography

[1] S. Zinkle and N. Ghoniem, 'Operating temperature windows for fusion reactor structural materials', *Fusion Engineering and Design*, vol. 51–52, pp. 55–71, 2000.

[2] A. Bhattacharya *et al.*, 'Irradiation damage concurrent challenges with RAFM and ODS steels for fusion reactor first-wall/blanket: a review', *Journal of Physics: Energy*, vol. 4, no. 3, p. 034003, Jul. 2022, doi: 10.1088/2515-7655/ac6f7f.

[3] A. Quadling, D. Bowden, C. Hardie, and A. Vasanthakumaran, 'Developing power plant materials using the life cycle lens', *Philosophical Transactions of the Royal Society A: Mathematical, Physical and Engineering Sciences*, vol. 382, no. 2280, p. 20230409, Aug. 2024, doi: 10.1098/rsta.2023.0409.

[4] A. Baker, 'The Spherical Tokamak for Energy Production (STEP) in context: UK public sector approach to fusion energy', *Philosophical Transactions of the Royal Society A: Mathematical, Physical and Engineering Sciences*, vol. 382, no. 2280, p. 20230401, Aug. 2024, doi: 10.1098/rsta.2023.0401.

[5] J. Yu, Y. Wu, J. Sha, Q. Huang, and Y. Ke, 'Neutron radiation effects of the center conductor post in a spherical tokamak reactor', *Journal of Nuclear Materials*, vol. 307–311, pp. 1670–1674, 2002, doi: https://doi.org/10.1016/S0022-3115(02)01106-6.

[6] S. J. Zinkle, '16 - Advanced irradiation-resistant materials for Generation IV nuclear reactors', in *Structural Materials for Generation IV Nuclear Reactors*, P. Yvon, Ed., Woodhead Publishing, 2017, pp. 569–594. doi: https://doi.org/10.1016/B978-0-08-100906-2.00016-1.

[7] H. Tanigawa *et al.*, 'Development of benchmark reduced activation ferritic/martensitic steels for fusion energy applications', *Nuclear Fusion*, vol. 57, no. 9, p. 092004, 2017, doi: 10.1088/1741-4326/57/9/092004.

[8] K. Shiba, H. Tanigawa, T. Hirose, and T. Nakata, ‘Development of the Toughness-Improved Reduced-Activation F82H Steel for DEMO Reactor’, *Fusion Science and Technology*, vol. 62, no. 1, pp. 145–149, Aug. 2012, doi: 10.13182/FST12-A14127.

[9] R. Lindau *et al.*, ‘Present development status of EUROFER and ODS-EUROFER for application in blanket concepts’, *Fusion Engineering and Design*, vol. 75–79, pp. 989–996, 2005, doi: https://doi.org/10.1016/j.fusengdes.2005.06.186.

[10] E. M. Ou Lahcen, M. M. Ángel Alcázar, and C. P. Almeida, ‘New high strength ODS Eurofer steel processed by mechanical alloying’, *Materials Science and Engineering: A*, vol. 817, p. 141288, 2021, doi: https://doi.org/10.1016/j.msea.2021.141288.

[11] L. Tan, Y. Katoh, and L. L. Snead, ‘Development of castable nanostructured alloys as a new generation RAFM steels’, *Journal of Nuclear Materials*, vol. 511, pp. 598–604, 2018, doi: https://doi.org/10.1016/j.jnucmat.2018.05.024.

[12] M. Klimenkov, R. Lindau, E. Materna-Morris, and A. Möslang, ‘TEM characterization of precipitates in EUROFER 97’, *Progress in Nuclear Energy*, vol. 57, pp. 8–13, 2012, doi: https://doi.org/10.1016/j.pnucene.2011.10.006.

[13] F. Hofer, P. Warbichler, B. Buchmayr, and S. Kleber, ‘On the detection of MX-precipitates in microalloyed steels using energy-filtering TEM’, *J Microsc*, vol. 184, no. 3, pp. 163–174, Dec. 1996, doi: https://doi.org/10.1046/j.1365-2818.1996.1240682.x.

[14] J. Haley *et al.*, ‘Short communication: Complete dissolution of MX-phase nanoprecipitates in fusion steels during irradiation by heavy-ions’, *Journal of Nuclear Materials*, vol. 596, p. 155115, 2024, doi: https://doi.org/10.1016/j.jnucmat.2024.155115.

[15] J. F. Ziegler, M. D. Ziegler, and J. P. Biersack, ‘SRIM - The Stopping and Range of Ions in Matter’, 2010.

[16] S. Agarwal, Y. Lin, C. Li, R. E. Stoller, and S. J. Zinkle, ‘On the use of SRIM for calculating vacancy production: Quick calculation and full-cascade options’, *Nucl Instrum Methods Phys Res B*, vol. 503, pp. 11–29, 2021, doi: https://doi.org/10.1016/j.nimb.2021.06.018.

[17] S. J. Bull, ‘Nanoindentation of coatings’, *J Phys D Appl Phys*, vol. 38, no. 24, pp. R393–R413, 2005, doi: https://doi.org/10.1088/0022-3727/38/24/R01.

[18] W. C. Oliver and G. M. Pharr, ‘Improved technique for determining hardness and elastic modulus using load and displacement sensing indentation experiments’, *J Mater Res*, vol. 7, no. 6, pp. 1564–1580, 1992.

[19] A. Leitner, V. Maier-Kiener, and D. Kiener, ‘Essential refinements of spherical nanoindentation protocols for the reliable determination of mechanical flow curves’, *Mater Des*, vol. 146, pp. 69–80, 2018, doi: https://doi.org/10.1016/j.matdes.2018.03.003.

[20] B. Merle, W. H. Higgins, and G. M. Pharr, ‘Critical issues in conducting constant strain rate nanoindentation tests at higher strain rates’, *J Mater Res*, vol. 34, no. 20, pp. 3495–3503, 2019, doi: 10.1557/jmr.2019.292.

[21] V. Maier, K. Durst, J. Mueller, B. Backes, H. W. Höppel, and M. Göken, ‘Nanoindentation strain-rate jump tests for determining the local strain-rate sensitivity in nanocrystalline Ni and ultrafine-grained Al’, *J Mater Res*, vol. 26, no. 11, pp. 1421–1430, 2011.

[22] H. Holz and B. Merle, ‘Novel nanoindentation strain rate sweep method for continuously investigating the strain rate sensitivity of materials at the nanoscale’, *Mater Des*, vol. 236, p. 112471, 2023, doi: https://doi.org/10.1016/j.matdes.2023.112471.

[23] P. Feldner, B. Merle, and M. Göken, ‘Determination of the strain-rate sensitivity of ultrafine-grained materials by spherical nanoindentation’, *J*

910 *Mater Res*, vol. 32, no. 8, pp. 1466–1473, 2017, doi: DOI:
911 10.1557/jmr.2017.69.

912 [24] S. Pathak and S. R. Kalidindi, 'Spherical nanoindentation stress-strain
913 curves', *Materials Science & Engineering R-Reports*, vol. 91, pp. 1–36,
914 2015, doi: 10.1016/j.mser.2015.02.001.

915 [25] W. Ramberg and W. R. Osgood, 'Description of Stress-Strain Curves by
916 Three Parameters', 1943. [Online]. Available:
917 https://api.semanticscholar.org/CorpusID:119534006

918 [26] G. Gadamchetty, A. Pandey, and M. Gawture, 'On Practical
919 Implementation of the Ramberg-Osgood Model for FE Simulation', *SAE*
920 *International Journal of Materials and Manufacturing*, vol. 9, no. 1, pp. 200–
921 205, 2016, [Online]. Available: http://www.jstor.org/stable/26268819

922 [27] P. Sudharshan Phani and W. C. Oliver, 'A critical assessment of the effect
923 of indentation spacing on the measurement of hardness and modulus
924 using instrumented indentation testing', *Mater Des*, vol. 164, p. 107563,
925 2019, doi: https://doi.org/10.1016/j.matdes.2018.107563.

926 [28] C. A. Schneider, W. S. Rasband, and K. W. Eliceiri, 'NIH Image to ImageJ: 25
927 years of image analysis', *Nat Methods*, vol. 9, no. 7, pp. 671–675, 2012, doi:
928 10.1038/nmeth.2089.

929 [29] F. Niessen, T. Nyyssönen, A. A. Gazder, and R. Hielscher, 'Parent grain
930 reconstruction from partially or fully transformed microstructures
931 in MTEX', *J Appl Crystallogr*, vol. 55, no. 1, pp. 180–194, Feb. 2022, doi:
932 10.1107/S1600576721011560.

933 [30] M. Duerrschnabel, U. Jäntsch, R. Gaisin, and M. Rieth, 'Microstructural
934 insights into EUROFER97 batch 3 steels', *Nuclear Materials and Energy*,
935 vol. 35, p. 101445, 2023, doi: https://doi.org/10.1016/j.nme.2023.101445.

936 [31] T. M. K. Green, T. Gräning, W. Zhong, Y. Yang, and K. G. Field, 'MX
937 precipitate behavior in an irradiated advanced Fe-9Cr steel: Self-ion

irradiation effects on phase stability', *Acta Mater*, vol. 296, p. 121203, 2025, doi: https://doi.org/10.1016/j.actamat.2025.121203.

[32] H. Tanigawa, H. Sakasegawa, H. Ogiwara, H. Kishimoto, and A. Kohyama, 'Radiation induced phase instability of precipitates in reduced-activation ferritic/martensitic steels', *Journal of Nuclear Materials*, vol. 367–370, pp. 132–136, 2007, doi: https://doi.org/10.1016/j.jnucmat.2007.03.155.

[33] S. Kano *et al.*, 'Instability of MX and M23C6 type precipitates in F82H steels under 2.8 MeV Fe2+ irradiation at 673 K', *Nuclear Materials and Energy*, vol. 17, pp. 56–61, 2018, doi: https://doi.org/10.1016/j.nme.2018.08.001.

[34] L. Tan, Y. Katoh, and L. L. Snead, 'Stability of the strengthening nanoprecipitates in reduced activation ferritic steels under Fe2+ ion irradiation', *Journal of Nuclear Materials*, vol. 445, no. 1, pp. 104–110, 2014, doi: https://doi.org/10.1016/j.jnucmat.2013.11.003.

[35] E. Gaganidze and J. Aktaa, 'Assessment of neutron irradiation effects on RAFM steels', *Fusion Engineering and Design*, vol. 88, no. 3, pp. 118–128, Mar. 2013, doi: 10.1016/j.fusengdes.2012.11.020.

[36] C. Heintze, C. Recknagel, F. Bergner, M. Hernandez-Mayoral, and A. Kolitsch, 'Ion irradiation induced damage of steels characterized by means of nanoindentation', *Nuclear Instruments and Methods in Physics Research, Section B*, vol. 267, p. 1505, 2009, [Online]. Available: http://ac.els-cdn.com/S0168583X09001220/1-s2.0-S0168583X09001220-main.pdf?_tid=9e559898-f6e5-11e3-8bc9-00000aacb361&acdnat=1403095361_0ffcc95f3ea4460b4cf7f3b592a159e8

[37] A. Das, E. Altstadt, C. Kaden, G. Kapoor, S. Akhmadaliev, and F. Bergner, 'Nanoindentation Response of Ion-Irradiated Fe, Fe-Cr Alloys and Ferritic-Martensitic Steel Eurofer 97: The Effect of Ion Energy', *Front Mater*, vol. 8, 2022, doi: 10.3389/fmats.2021.811851.

966 [38] C. Couchet *et al.*, ‘Recovery of severely deformed ferrite studied by in situ
967 high energy X-ray diffraction’, *Mater Charact*, vol. 179, p. 111378, Sep.
968 2021, doi: 10.1016/j.matchar.2021.111378.

969 [39] P. Marmy, J. L. Martin, and M. Victoria, ‘Deformation mechanisms of a
970 ferritic-martensitic steel between 290 and 870 K’, *Materials Science and*
971 *Engineering: A*, vol. 164, no. 1, pp. 159–163, 1993, doi:
972 https://doi.org/10.1016/0921-5093(93)90654-W.

973 [40] J. K. Engels *et al.*, ‘Indentation size effects in spherical nanoindentation
974 analyzed by experiment and non-local crystal plasticity’, *Materialia (Oxf)*,
975 vol. 3, pp. 21–30, 2018, doi: https://doi.org/10.1016/j.mtla.2018.09.032.

976 [41] I. Sacksteder, H.-C. Schneider, and E. Materna-Morris, ‘Determining
977 irradiation damage and recovery by instrumented indentation in RAFM
978 steel’, *Journal of Nuclear Materials*, vol. 417, no. 1, pp. 127–130, 2011, doi:
979 https://doi.org/10.1016/j.jnucmat.2011.02.012.

980 [42] A. Puype, L. Malerba, N. De Wispelaere, R. Petrov, and J. Sietsma, ‘Effect of
981 processing on microstructural features and mechanical properties of a
982 reduced activation ferritic/martensitic EUROFER steel grade’, *Journal of*
983 *Nuclear Materials*, vol. 494, pp. 1–9, 2017, doi:
984 https://doi.org/10.1016/j.jnucmat.2017.07.001.

985 [43] L. Tan, Y. Yang, and J. T. Busby, ‘Effects of alloying elements and
986 thermomechanical treatment on 9Cr Reduced Activation Ferritic–
987 Martensitic (RAFM) steels’, *Journal of Nuclear Materials*, vol. 442, no. 1,
988 Supplement 1, pp. S13–S17, 2013, doi:
989 https://doi.org/10.1016/j.jnucmat.2012.10.015.

990 [44] C. Celada-Casero, J. Sietsma, and M. J. Santofimia, ‘The role of the
991 austenite grain size in the martensitic transformation in low carbon steels’,
992 *Mater Des*, vol. 167, p. 107625, 2019, doi:
993 https://doi.org/10.1016/j.matdes.2019.107625.

[45] S. J. Zinkle and L. L. Snead, ‘Designing Radiation Resistance in Materials for Fusion Energy*’, *Annu Rev Mater Res*, vol. 44, no. Volume 44, 2014, pp. 241–267, 2014, doi: https://doi.org/10.1146/annurev-matsci-070813-113627.

[46] D. Brimbal *et al.*, ‘Microstructural characterization of Eurofer-97 and Eurofer-ODS steels before and after multi-beam ion irradiations at JANNUS Saclay facility’, *Journal of Nuclear Materials*, vol. 465, pp. 236–244, 2015, doi: https://doi.org/10.1016/j.jnucmat.2015.05.045.

[47] A. Bhattacharya *et al.*, ‘Irradiation damage concurrent challenges with RAFM and ODS steels for fusion reactor first-wall/blanket: a review’, *Journal of Physics: Energy*, vol. 4, no. 3, p. 034003, 2022, doi: 10.1088/2515-7655/ac6f7f.

[48] C. D. Hardie, C. A. Williams, S. Xu, and S. G. Roberts, ‘Effects of irradiation temperature and dose rate on the mechanical properties of self-ion implanted Fe and Fe–Cr alloys’, *Journal of Nuclear Materials*, vol. 439, no. 1, pp. 33–40, 2013, doi: https://doi.org/10.1016/j.jnucmat.2013.03.052.

[49] C. Heintze, F. Bergner, M. Hernández-Mayoral, R. Kögler, G. Müller, and A. Ulbricht, ‘Irradiation hardening of Fe–9Cr-based alloys and ODS Eurofer: Effect of helium implantation and iron-ion irradiation at 300 °C including sequence effects’, *Journal of Nuclear Materials*, vol. 470, pp. 258–267, 2016, doi: https://doi.org/10.1016/j.jnucmat.2015.12.041.

[50] C. Dethloff, E. Gaganidze, and J. Aktaa, ‘Quantitative TEM analysis of precipitation and grain boundary segregation in neutron irradiated EUROFER97’, *Journal of Nuclear Materials*, vol. 454, no. 1, pp. 323–331, 2014, doi: https://doi.org/10.1016/j.jnucmat.2014.07.078.

[51] L. Tan and J. T. Busby, ‘Formulating the strength factor α for improved predictability of radiation hardening’, *Journal of Nuclear Materials*, vol. 465, pp. 724–730, 2015, doi: https://doi.org/10.1016/j.jnucmat.2015.07.009.

[52] P. Zhang, S. X. Li, and Z. F. Zhang, ‘General relationship between strength and hardness’, *Materials Science and Engineering: A*, vol. 529, pp. 62–73, 2011, doi: https://doi.org/10.1016/j.msea.2011.08.061.

[53] J. Kappacher, O. Renk, D. Kiener, H. Clemens, and V. Maier-Kiener, ‘Controlling the high temperature deformation behavior and thermal stability of ultra-fine-grained W by re alloying’, *J Mater Res*, vol. 36, no. 12, pp. 2408–2419, 2021, doi: 10.1557/s43578-020-00026-z.

[54] R. G. Abernethy *et al.*, ‘Effects of neutron irradiation on the brittle to ductile transition in single crystal tungsten’, *Journal of Nuclear Materials*, p. 151799, 2019.

[55] S. Takeuchi, ‘Solid-Solution Strengthening in Single Crystals of Iron Alloys’, *J Physical Soc Japan*, vol. 27, no. 4, pp. 929–940, Oct. 1969, doi: 10.1143/JPSJ.27.929.

[56] J. S.-L. Gibson, S. Schröders, C. Zehnder, and S. Korte-Kerzel, ‘On extracting mechanical properties from nanoindentation at temperatures up to 1000° C’, *Extreme Mech Lett*, vol. 17, pp. 43–49, 2017.

[57] J. S. Weaver *et al.*, ‘Spherical nanoindentation of proton irradiated 304 stainless steel: A comparison of small scale mechanical test techniques for measuring irradiation hardening’, *Journal of Nuclear Materials*, vol. 493, pp. 368–379, 2017, doi: https://doi.org/10.1016/j.jnucmat.2017.06.031.

[58] I. S. Yasnikov, A. Vinogradov, and Y. Estrin, ‘Revisiting the Considère criterion from the viewpoint of dislocation theory fundamentals’, *Scr Mater*, vol. 76, pp. 37–40, 2014, doi: https://doi.org/10.1016/j.scriptamat.2013.12.009.

[59] K. Song, H. Yu, P. Karamched, K. Mizohata, D. E. J. Armstrong, and F. Hofmann, ‘Deformation behaviour of ion-irradiated FeCr: A nanoindentation study’, *J Mater Res*, vol. 37, no. 12, pp. 2045–2060, 2022, doi: 10.1557/s43578-022-00613-2.

[60] M. Matijasevic and A. Almazouzi, ‘Effect of Cr on the mechanical properties and microstructure of Fe–Cr model alloys after n-irradiation’, *Journal of Nuclear Materials*, vol. 377, no. 1, pp. 147–154, 2008, doi: https://doi.org/10.1016/j.jnucmat.2008.02.061.

[61] E. Gaganidze, F. Gillemot, I. Szenthe, M. Gorley, M. Rieth, and E. Diegele, ‘Development of EUROFER97 database and material property handbook’, *Fusion Engineering and Design*, vol. 135, pp. 9–14, 2018, doi: https://doi.org/10.1016/j.fusengdes.2018.06.027.

[62] N. P. Taylor, P. J. Knight, and D. J. Ward, ‘A model of the availability of a fusion power plant’, *Fusion Engineering and Design*, vol. 51–52, pp. 363–369, 2000, doi: https://doi.org/10.1016/S0920-3796(00)00296-9.

[63] A. Bhattacharya *et al.*, ‘Irradiation hardening and ductility loss of Eurofer97 steel variants after neutron irradiation to ITER-TBM relevant conditions’, *Fusion Engineering and Design*, vol. 173, p. 112935, 2021, doi: https://doi.org/10.1016/j.fusengdes.2021.112935.